



Revealing interfacial charge redistribution of homologous Ru-RuS₂ heterostructure toward robust hydrogen oxidation reaction

Yi Liu^a, Lianrui Cheng^a, Shuqing Zhou^a, Yuting Yang^a, Chenggong Niu^a, Tayirjan Taylor Isimjan^{c,*}, Bao Wang^{b,*}, Xiulin Yang^{a,*}

^aGuangxi Key Laboratory of Low Carbon Energy Materials, School of Chemistry and Pharmaceutical Sciences, Guangxi Normal University, Guilin 541004, Guangxi, China

^bState Key Laboratory of Biochemical Engineering, Institute of Process Engineering, Chinese Academy of Sciences, Beijing 100190, China

^cSaudi Arabia Basic Industries Corporation (SABIC) at King Abdullah University of Science and Technology (KAUST), Thuwal 23955-6900, Saudi Arabia

ARTICLE INFO

Article history:

Received 11 December 2023

Revised 2 March 2024

Accepted 9 March 2024

Available online 18 March 2024

Keywords:

Heterostructure

Hollow spherical structure

Hydrogen oxidation reaction

Charge redistribution

Density functional calculation

ABSTRACT

Precisely tailoring the surface electronic structures of electrocatalysts for optimal hydrogen binding energy and hydroxide binding energy is vital to improve the sluggish kinetics of hydrogen oxidation reaction (HOR). Herein, we employ a partial desulfurization strategy to construct a homologous Ru-RuS₂ heterostructure anchored on hollow mesoporous carbon nanospheres (Ru-RuS₂@C). The disparate work functions of the heterostructure contribute to the spontaneous formation of a unique built-in electric field, accelerating charge transfer and boosting conductivity of electrocatalyst. Consequently, Ru-RuS₂@C exhibits robust HOR electrocatalytic activity, achieving an exchange current density and mass activity as high as 3.56 mA cm⁻² and 2.13 mA μg_{Ru}⁻¹, respectively, exceeding those of state-of-the-art Pt/C and most contemporary Ru-based HOR electrocatalysts. Surprisingly, Ru-RuS₂@C can tolerate 1000 ppm of CO that lacks in Pt/C. Comprehensive analysis reveals that the directional electron transfer across Ru-RuS₂ heterointerface induces local charge redistribution in interfacial region, which optimizes and balances the adsorption energies of H and OH species, as well as lowers the energy barrier for water formation, thereby promoting the HOR performance.

© 2024 Science Press and Dalian Institute of Chemical Physics, Chinese Academy of Sciences. Published by ELSEVIER B.V. and Science Press. All rights reserved.

1. Introduction

Benefitting from their superior H₂ utilization efficiency and eco-friendly emission, hydrogen fuel cell technologies are deemed critical in driving the low-carbon-emission hydrogen economy [1,2]. Among various fuel cells, proton exchange membrane fuel cell (PEMFC) and alkaline exchange membrane fuel cells (AEMFC) stand out as the primary techniques for hydrogen utilization [3,4]. However, the widespread adoption of PEMFC is inevitably thwarted by expensive Pt-based materials and per-fluorinated membranes [5,6]. AEMFCs, as a potentially more cost-effective substitute, have gained significant interest for their allowable use of more economical air loops and bipolar plates, along with operating in less-corrosive alkaline environment [7,8]. Regrettably, the kinetics of anodic hydrogen oxidation reaction (HOR) in

AEMFCs is decreased substantially when transitioning from acidic to alkaline medium [9,10]. Hence, exploiting efficient and cost-effective HOR electrocatalysts in alkaline medium remains a key pursuit in advancing AEMFCs.

Ruthenium (Ru) has stimulated substantial attention by merits of its suitable Ru–H bond strength, higher CO tolerance, as well as more extensive reserves than Pt [10,11], and its HOR activity may be boosted to rival or even surpass the state-of-the-art Pt/C after fine-tuning [9,12]. Generally, the electrocatalytic performance of catalysts largely hinges on the surface charge states of the building materials [13,14]. Adjusting these states through surface modifications involving phase control [15], heteroatom doping [16,17], and heterointerface construction [18,19] is a productive strategy. In particular, heterojunction systems constructed by two phases with disparate work functions (WF) can generate a built-in electric field (BEF) with varying surface charge distributions at the interface, which promotes electron transport during the electrocatalytic process and fine-tune the electronic structure of the catalysts, leading to optimized hydrogen binding energy (HBE) [20–22]. For instance, Li et al. constructed polymorphism-interfaced

* Corresponding authors.

E-mail addresses: isimjant@sabic.com (T.T. Isimjan), baowang@ipe.ac.cn (B. Wang), xlyang@gxnu.edu.cn (X. Yang).

fcc-hcp-Ru nanocatalysts with significant WF differences. The unique built-in electric field at the polycrystalline interface enables it to yield remarkable HOR performance [23]. It is therefore anticipated that heterostructure composed of Ru-based compounds with appropriate interfacial coupling effects will significantly improve intrinsic catalytic activity for HOR.

In light of above factors, we created an innovative Ru-RuS₂ heterostructure encased in three-dimensional (3D) hollow mesoporous carbon nanospheres via a partial desulfurization strategy. This unique hollow mesoporous structure established a viable three-phase interface and offered a larger specific surface area, minimizing the diffusion resistance and exposing more active sites. As expected, the resulting Ru-RuS₂@C heterostructure performed considerable catalytic activity toward HOR in the alkaline electrolyte. Moreover, the Ru-RuS₂@C also demonstrated a commendable long-term stability, along with exceptional CO tolerance. Experimental and theoretical findings collectively confirmed that the charge redistribution at the interface derived from the differing WF of the two species on tunable Ru-RuS₂, which resulted in weakened HBE and improved hydroxide binding energy (OHBE), thereby substantially improving HOR performance in alkaline electrolytes.

2. Experimental

2.1. Reagents and materials

All chemicals and reagents were utilized as purchased without any further purification. These included tetraethyl silicate (TEOS), ammonia solution (NH₄OH), 3-hydroxytyramine hydrochloride (C₈H₁₁NO₂-HCl), ruthenium trichloride (RuCl₃·xH₂O, AR, 99%, ~40 wt% Ru), L-cysteine (C₃H₇NO₂S, AR, 99%), ethanol absolute (AR, 99.5%), commercial Pt/C (20 wt% Pt), nafion solution (5 wt%), and potassium hydroxide (KOH, AR, >90%). The deionized water (18.25 MΩ cm⁻¹) from a water purification system (Ulupure) was used throughout the whole experiment.

2.2. Preparation of 3D hollow mesoporous carbon nanospheres (HMCN)

HMCN were fabricated based on previously reported work with slightly modification [24]. Specifically, 5 mL of TEOS was rapidly added to a mixed solution of ethanol (100 mL), deionized water (30 mL), and NH₄OH (5 mL) under vigorous stirring. After 1 h, 500 mg of 3-hydroxytyramine hydrochloride was introduced to the mixture, and stirred for another 12 h at room temperature. The black powder was harvested via centrifugation, washed several times with deionized water and ethanol, and dried overnight at 60 °C. The obtained sample was then annealed in a N₂ atmosphere at 400 °C for 2 h with a ramp rate of 5 °C min⁻¹, and subsequently heated to 800 °C for 3 h to acquire SiO₂ spheres. Finally, HMCN were prepared by thoroughly removing SiO₂ with 3 M NaOH.

2.3. Preparation of Ru-RuS₂@C hollow heterostructure, RuS₂@C and Ru@C

Typically, a specific amount of HMCN was dispersed in 70 mL of mixed solution (deionized water: ethylene glycol: ethanol = 3:1:1 v/v/v) containing 30 mg RuCl₃·xH₂O and 73.5 mg C₃H₇NO₂S, and then sonicated for 30 min to uniformly disperse the carbon spheres in the solution. The mixture was then transferred to a 100 mL Teflon-lined autoclave and heated at 160 °C for 9 h. The resulting Ru-RuS₂@C hollow heterostructure was harvested by centrifugation, washed several times with ethanol, and dried in vacuum oven overnight. The precursor was then annealed at 800 °C for 2 h at a

heating rate of 5 °C min⁻¹ in an Ar atmosphere. After naturally cooling, the obtained sample was denoted as Ru-RuS₂@C, with a specific Ru content of 4.95 wt%, which was verified by inductively coupled plasma (ICP) measurements.

As a control, the synthesis of RuS₂@C was similar to that of Ru-RuS₂@C, except that the temperature was changed to 700 °C. Contemporary, Ru@C can be obtained without adding S source (L-cysteine).

3. Results and discussion

3.1. Synthesis and structural characterization

The Ru-RuS₂@C heterostructure was synthesized through hydrothermal and high-temperature carbonization approaches to load Ru-RuS₂ species onto 3D hollow mesoporous carbon nanospheres (HMCN). Specifically, RuCl₃ precursor and L-cysteine (C₃H₇NO₂S) were sonically dissolved in a mixed solvent containing a certain amount of HMCN to produce pre-Ru-S@C via a straightforward hydrothermal process. The HMCN with a large accessible inner cavity can accommodate foreign active metals effectively [3]. Ultimately, the resulting pre-Ru-S@C hybrid was annealed under argon to activate the metal sites to obtain Ru-RuS₂@C heterostructure (Fig. 1a). Counterparts, RuS₂@C and Ru@C were fabricated using a similar method. The X-ray diffraction (XRD) patterns of the Ru-RuS₂@C, RuS₂@C, and Ru@C catalysts were revealed in Fig. 1(b). The diffraction peaks of RuS₂@C and Ru@C matched the RuS₂ phase (JCPDS: 80-0669) and Ru phase (JCPDS: 88-1734), respectively. The peaks of the Ru-RuS₂@C compound was indexed to above RuS₂ and Ru phase, indicative of the successful formation of Ru-RuS₂ heterostructure. Notably, the XRD pattern of Ru-RuS₂@C revealed a high angular shift of the characteristic peak (101) of Ru, indicating a decrease in the unit volume of the Ru lattice. This variation may be attributed to the doping of RuS₂ into Ru, forming a Ru-RuS₂ heterostructure, which led to the contraction of the Ru lattice. To validate the preparation of a single RuS₂@C component, we conducted additional XRD analyses at various temperatures (Fig. S1). Results indicated that Ru diffraction peaks began to emerge and increased at temperatures equal to or greater than 750 °C. Conversely, it showed no signs of metallic Ru peaks when the temperature was at or below 700 °C. Subsequent analysis of high-resolution image (Fig. S2) of samples calcined at 700 °C revealed lattice fringes exclusively attributable to RuS₂, with no detected lattice fringes indexed to metallic Ru. Consequently, we designated samples calcined at 700 °C as single RuS₂@C.

Scanning electron microscopy (SEM) and transmission electron microscopy (TEM) were employed to probe the morphology of Ru-RuS₂@C. As depicted in Fig. S3, SiO₂@DA (DA: dopamine) showed a monodispersed spherical morphology. After annealing and wiping off nucleated SiO₂ by alkali-steeping, the original solid spherical evolved into the hollow nanospheres with smooth surfaces and uniform dispersion (Fig. S4). Especially, upon loading the Ru-RuS₂ heterojunction onto HMCN, its morphology was well inherited (Fig. 1c). With the elimination of the inert lumpy interior, the monodispersed hollow spherical morphology offers a merit over a solid sphere in reducing the transport distance of the reactants [24]. Further TEM observations in Fig. 1(d) confirmed the hollow spherical nature of Ru-RuS₂@C. In Fig. S5 and the illustration, the Ru-RuS₂ particles were evenly distributed throughout the entire hollow structure, exhibiting a small average particle size of 2.82 nm. Benefiting from the synergistic effect between Ru and RuS₂ species, Ru-RuS₂@C encapsulated ideal nanoscale Ru-RuS₂ heterojunction particles homogeneously anchored on the carbon carrier, significantly improving atom utilization efficiency and catalytic activity. In contrast, single component such as RuS₂@C

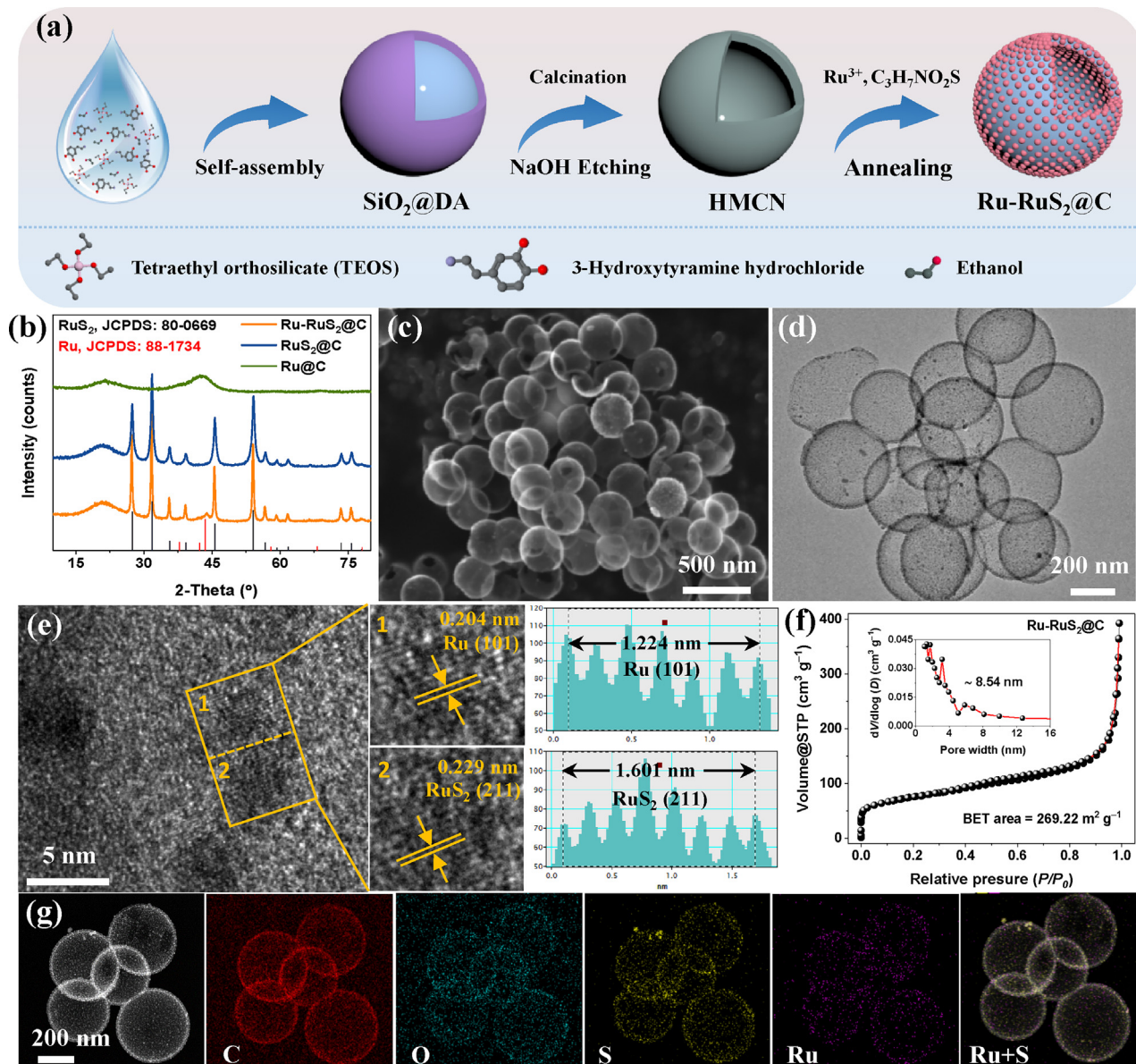


Fig. 1. (a) Schematic illustration of the preparation of Ru-RuS₂@C. (b) XRD patterns of Ru-RuS₂@C, RuS₂@C, and Ru@C. (c) SEM and (d) TEM images of Ru-RuS₂@C. (e) High-resolution TEM image and corresponding lattice fringes of Ru-RuS₂@C. (f) N₂ adsorption-desorption isotherms and pore size distribution (inset) of Ru-RuS₂@C. (g) Elemental mappings of Ru-RuS₂@C.

(~6.06 nm) or Ru@C (~4.99 nm) tends to agglomerate on the carrier, resulting in a significantly larger nanoparticle size of the surface particles. This agglomeration phenomenon may cover many active sites, leading to inferior electrochemical performance compared to Ru-RuS₂@C. High-resolution TEM (HRTEM) image inspection (Fig. 1e) revealed the lattice fringes of 0.204 and 0.229 nm at the Ru-RuS₂ heterogeneous interface, corresponding to the (101) plane of Ru and the (211) plane of RuS₂, respectively. N₂ adsorption/desorption isotherm indicated the IV-type curves with an apparent hysteresis loop, suggesting the mesoporosity of Ru-RuS₂@C nanospheres (Fig. 1f) [25]. This mesoporosity might be related to the etching of SiO₂ core. Furthermore, Ru-RuS₂@C possessed the highest Brunauer-Emmett-Teller (BET) surface area of 269.22 m² g⁻¹ compared to RuS₂@C (244.44 m² g⁻¹) and Ru@C (218.02 m² g⁻¹), which aided in increasing the attainability of active sites (Fig. S6) [26]. To showcase the superiority of the hollow structure carriers, we substituted XC-72R carbon black and unetched silica solid spheres for comparison. Evidently, the specific

surface area of Ru-RuS₂@C significantly exceeds that of Ru-RuS₂@XC-72R and Ru-RuS₂@SiO₂. The mesoporous structure of Ru-RuS₂@C was further verified by pore-size distribution, which could be beneficial for H₂ molecule adsorption and the electrons/mass transport in the heterogeneous interface, thus strengthening its catalytic performance [27]. As exhibited in Fig. 1(g), the high-angle annular dark-field scanning TEM (HAADF-STEM)-energy dispersive X-ray mappings indicated the coexistence of C, O, S, and Ru elements throughout the whole heterostructure.

Raman spectra of the as-synthesized three catalysts were plotted in Fig. S7. Broad D (~1342 cm⁻¹) and G (~1588 cm⁻¹) bands generally reflected the disorder/defects and graphitization degree of carbon species, respectively. Ru-RuS₂@C presented the lowest I_D/I_G values compared to RuS₂@C (0.86) and Ru@C (0.91), implying that Ru-RuS₂@C had more sp² hybridized carbon, facilitating accelerated charge transfer [28]. X-ray photoelectron spectroscopy (XPS) was carried out to elucidate the surface constitution and chemical states of the samples [29]. XPS survey spectrum

(Fig. S8) of Ru-RuS₂@C further affirmed the presence of C, O, S, and Ru elements. Fig. 2(a) showed the high-resolution Ru 3p XPS spectrum of Ru-RuS₂@C. The deconvoluted peaks situated at approximately 461.1 and 483.4 eV corresponded to the 3p_{3/2} and 3p_{1/2} orbitals of metallic Ru, respectively, while the peaks situated around 464.1 and 487.4 eV accounted for the 3p_{3/2} and 3p_{1/2} of Ru⁴⁺ [30]. For comparison, the binding energy of Ru species in Ru-RuS₂@C was lower than that in pure Ru@C, but higher than that in RuS₂@C, indicating the electron interaction between Ru and RuS₂, which further verified the formation of Ru-RuS₂ heterostructure (Fig. 2b). This suggested the electron transfer from RuS₂ to Ru. With respect to the S 2p XPS spectra (Fig. 2c), four independent subpeaks were concentrated at 162.27, 163.42, 164.32, and 167.79 eV, associating with the 2p_{3/2} and 2p_{1/2} of Ru-S, C-S-C, and S-O species, respectively [21]. To deeply profile the effect of heterogeneous interfaces on HOR activity, ultraviolet photoelectron spectroscopy (UPS) was conducted to determine the work function (WF) of different materials. As exhibited in Fig. 2(d) and the illustration, the WF values of RuS₂@C and Ru@C were determined to be 4.22 and 4.56 eV, respectively, further corroborating the surface electron transfer from RuS₂ to Ru. Owing to the discrepant WF at the two-phase interface, a built-in electric field (BEF) was formed, and the electrons at the interface were transferred from high to low positions, resulting in a redistribution of surface charge density (Fig. 2e) [23]. Furthermore, we measured the work function of Ru-RuS₂@C heterostructures (Fig. S9). Relative to RuS₂@C and Ru@C, the decrease in the WF value of Ru-RuS₂@C heterogeneous catalysts can reduce the zero-charge potential and promote alkaline HOR at a lower interfacial water reionization barrier [31].

3.2. Electrochemical HOR performance

The role of heterogeneous engineering in electrocatalysis was explored by systematically investigating the HOR electrocatalytic properties using a standard three-electrode technique. The reversible hydrogen electrode (RHE) calibration was conducted before measurements (Fig. S10). All electrochemical data of HOR were

iR-corrected (Fig. S11). Initially, we examined the impact of varying reaction conditions on the catalytic performance of Ru-RuS₂@C. The optimal reaction temperature of Ru-RuS₂@C was fixed at 800 °C (Fig. S12). Speak of the effect of Ru content, we noted a distinct volcano-shaped trend in catalytic performance, peaking at 4.95 wt% Ru loading (Fig. S13 and Table S1). Suboptimal performance below this level suggested inadequate active sites, while excessive Ru led to species agglomeration, covering active sites. The optimal Ru content likely facilitated uniform distribution of Ru-RuS₂ heterojunctions, maximizing active site exposure. The finding was consistent with previous reports [32]. Additionally, we optimized the support and identified hollow multihole carbon spheres as the optimal carrier for this study (Fig. S14). Generally, the peaks of hydrogen under-potential deposition (H_{upd}) on the cyclic voltammetry (CV) curve directly related to the HBE. The peak at lower potential in the H_{upd} region corresponded to attenuated HBE, which was more favorable for HOR [3,33]. In Fig. S15, the H_{upd} peak potentials of Ru-RuS₂@C were more negative than that of Pt/C, reflecting the weaker hydrogen adsorption ability on Ru sites. On the contrary, RuS₂@C and Ru@C showed the unremarkable H_{upd} peaks, suggesting that the strong electronic interaction between RuS₂ and Ru species can weaken the HBE [34]. Linear sweep voltammetry (LSV) was executed to achieve HOR polarization curves for various electrocatalysts in H₂-saturated 0.1 M KOH (Fig. 3a). Ru-RuS₂@C exhibited the highest anodic current density throughout the potential range, and the onset potential as low as 0 V vs. RHE. This extraordinary capacity even exceeded that of commercial Pt/C. We further recorded the HOR polarization curve in N₂-saturated electrolyte as a control experiment (Fig. S16). Ru-RuS₂@C revealed a negligible current-voltage feature, affirming that anode current mainly rooted in H₂ oxidation rather than other species in the system [35]. Furthermore, we measured the HOR polarization curves of Ru-RuS₂@C at different rotating speeds to analyze the catalytic process (Fig. 3b), where the limiting current density increased with increasing rotational rate, verifying a H₂ mass-transfer-controlled process [12,36]. The Koutecky-Levich (K-L) plot at 50 mV vs. RHE yielded a slope of 4.59 cm² mA⁻¹ s^{-1/2} (theoretical slope value of ~4.87 cm² mA⁻¹ s^{-1/2}), corroborating

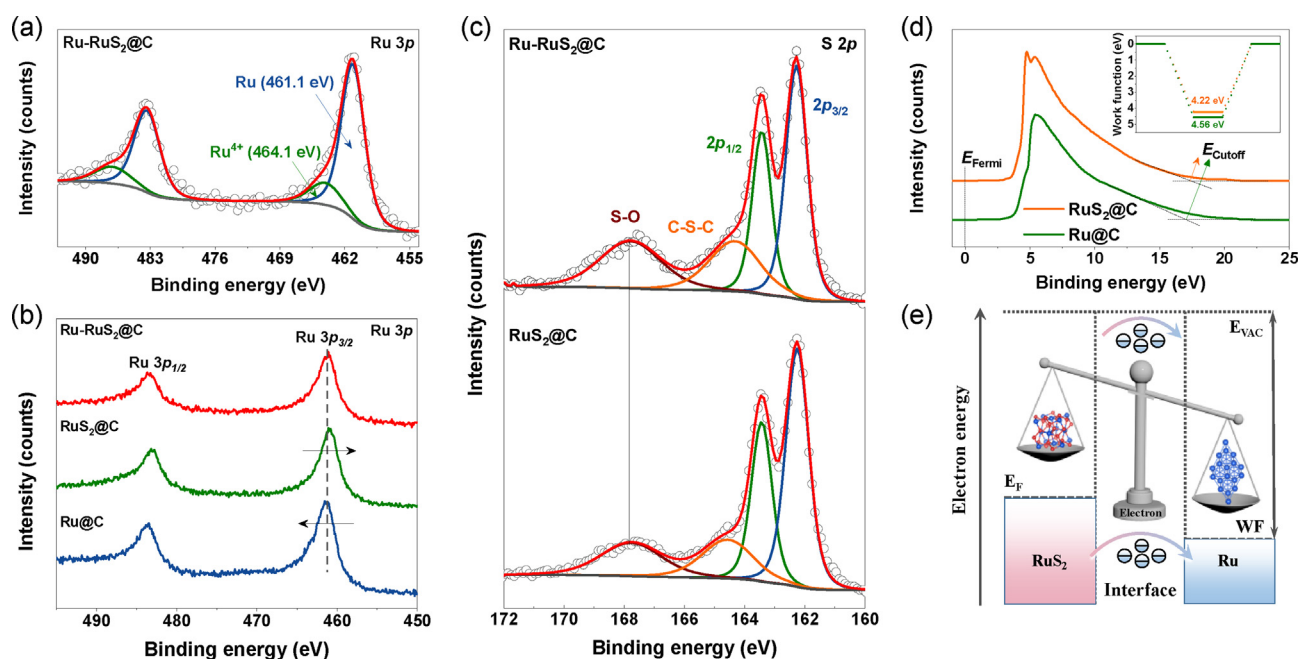


Fig. 2. High resolution XPS of Ru 3p in (a) Ru-RuS₂@C, (b) Ru-RuS₂@C, RuS₂@C, and Ru@C. (c) High resolution XPS of S 2p in Ru-RuS₂@C and RuS₂@C. (d) UPS spectra of the RuS₂@C and Ru@C and corresponding work function. (e) Schematic illustration of the built-in electric field and charge redistribution.

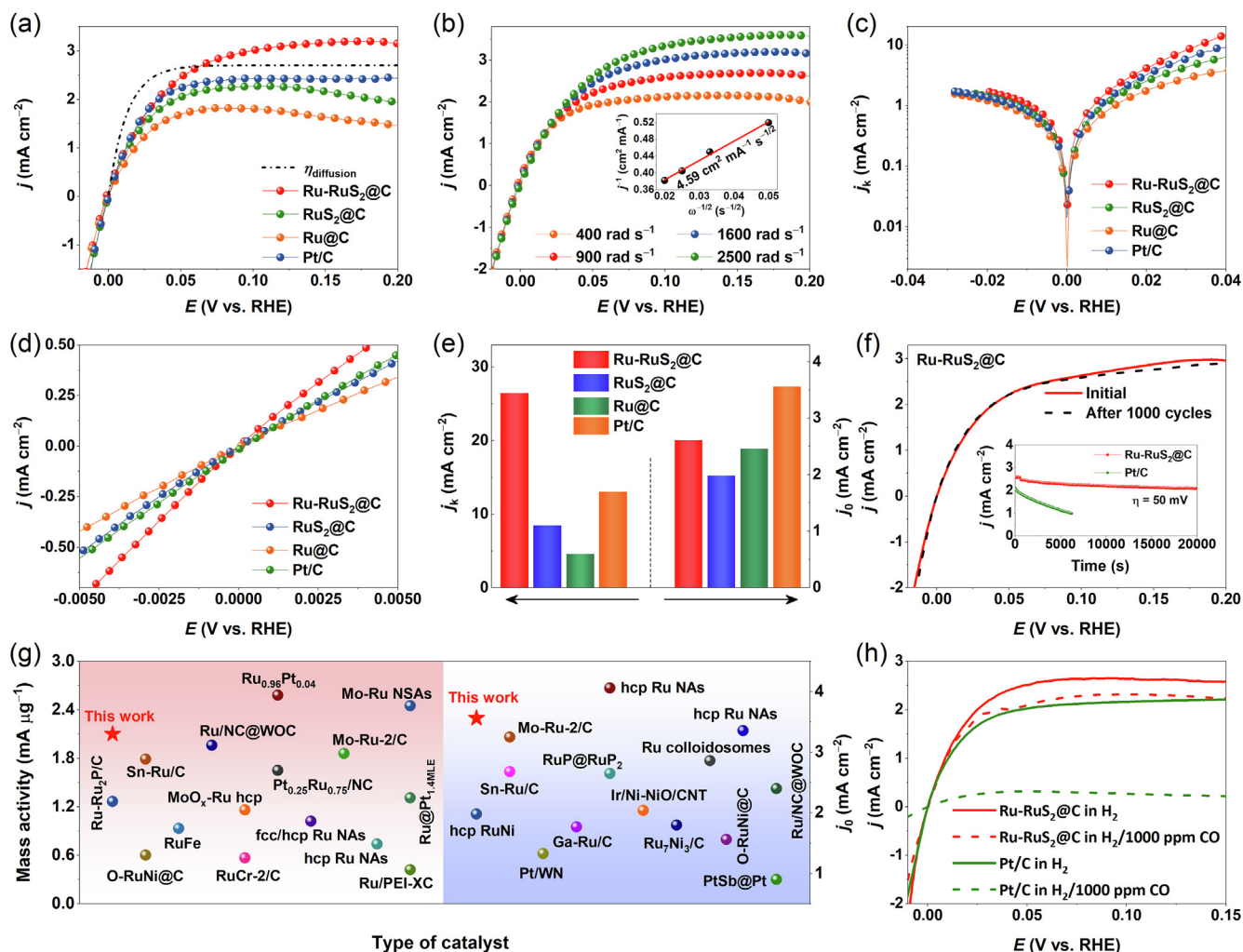


Fig. 3. (a) HOR polarization curves in H_2 -saturated 0.1 M KOH at a scan rate of 10 mV s^{-1} and a rotating speed of 1600 r min^{-1} . (b) Polarization curves of Ru-RuS₂@C at different rotation speeds. Inset shows corresponding Koutecky-Levich plot. (c) Tafel plots. (d) Linear fitting curves in micropolarization region. (e) Comparison of j_k and j_0 of the studied electrocatalysts. (f) Accelerated durability test and chronoamperometric curve at 50 mV response of Ru-RuS₂@C. (g) Comparison of the mass activity and j_0 with other recently reported alkaline HOR electrocatalysts. (h) Polarization curves of Ru-RuS₂@C and commercial Pt/C in 1000 ppm CO/ H_2 -saturated 0.1 M KOH.

that the HOR electrolysis on Ru-RuS₂@C abided by an approximate two-electron transfer HOR process (Fig. 3b and the insert).

Fig. 3(c) summarized the kinetic currents (j_k) of all studied catalysts at 50 mV, and the Ru-RuS₂@C displayed the highest geometric j_k (26.48 mA cm^{-2}) compared to RuS₂@C (8.46 mA cm^{-2}), Ru@C (4.62 mA cm^{-2}), and Pt/C (13.03 mA cm^{-2}), proving the quickest HOR kinetics on Ru-RuS₂@C [37]. Subsequently, we calculated the exchange current density (j_0) by extracting linear fit data in micropolarization range according to the simplified Butler-Volmer formula (Fig. 3d). As anticipated, Ru-RuS₂@C reached the desired geometric j_0 of 3.56 mA cm^{-2} , suggesting the remarkable inherent activity of Ru-RuS₂@C (Fig. 3e and Table S2) [38]. An accelerated durability test (ADT) was operated by performing 1000 CV cycles (Fig. 3f) and chronoamperometry ($j-t$) measurements (insert in Fig. 3f) in 0.1 M H_2 -saturated KOH electrolyte. It was unexpected to observe nearly overlapping polarization curves for the two HOR conditions after 1000 cycles. Moreover, the limiting current density showed only a slight decrease even after 5000 cycles (Fig. S17). Meanwhile, Ru-RuS₂@C showed only a slight current density decay, contrasting sharply with the significant decline observed in commercial Pt/C, which suggested the durable stability of Ru-RuS₂@C. In Fig. S18, Ru-RuS₂@C-After HOR retained its initial morphology with some structural collapse. Meanwhile, we also

found that the signals of Ru, Ru⁴⁺, and S were still present in Ru-RuS₂@C after 1000 CVs (Fig. S19). These findings affirmed the robust surface structure of the catalysts, safeguarding the active center against alkali corrosion during HOR. It is worth noting that the mass activity ($2.13 \text{ mA } \mu\text{g}_{\text{Pt}}^{-1}$) at 50 mV and exchange current density of Ru-RuS₂@C substantially surpassed most documented Ru-based catalysts (Fig. 3g and Table S3). Due to the inevitable infiltration of CO impurity in hydrogen fuel systems, CO tolerance was another crucial characteristic for evaluating high-efficiency HOR catalysts [39]. As illustrated in Fig. 3(h), the anodic current density of commercial Pt/C declined sharply compared with the incipient state. This result explained that the active sites on the catalytic surface were almost occupied or poisoned by CO, which consequently impeded the sites for hydrogen adsorption/dissociation [40]. As a stark contrast, the LSV polarization curve of Ru-RuS₂@C was basically consistent with the initial curve even at the same CO concentration as that of Pt/C catalysts, implying an admirable tolerance and resistance to CO poisoning [41].

Given the high hydrogen concentration in the H adsorption/desorption potential region, Ru is easily oxidized and it is not suitable to calculate electrochemistry active surface area (ECSA) by measuring the charge associated with this region [42]. Contemporary, numerous research had manifested that OH_{ad} species can expedite

the removal of CO_{ad} intermediates on metal surfaces, and the CO stripping potential was directly associated with the strength of OH^- adsorption [43]. Therefore, CO-stripping experiments were performed to determine the ECSA values and monitor the $^*\text{OH}$ binding strength on the studied catalysts. As demonstrated in Fig. 4(a and b), an ECSA value of Ru-RuS₂@C was assessed to be 75.14 m² g⁻¹, which was higher than that of RuS₂@C (36.72 m² g⁻¹), Ru@C (47.28 m² g⁻¹), and commercial Pt/C (38.71 m² g⁻¹). A higher ECSA represented more catalytic reactive sites, which favored the close contact between reactants and electrolyte [44]. As shown in Fig. 4(c and d) and Fig. S20, compared with the RuS₂@C (0.67 V) and Ru@C (0.71 V), the peak potential of CO stripping on Ru-RuS₂@C heterostructure (0.58 V) was smaller. Moreover, Ru-RuS₂@C (-20.76 mV) had more negative zeta potential than RuS₂@C (-16.34 mV) and Ru@C (-11.52 mV). All of these observations reflected that all these catalysts interacted with OH^* , and demonstrated the strongest OHBE on Ru-RuS₂@C. Interestingly, the order of OHBE (Ru-RuS₂@C > RuS₂@C > Ru/C) matched the trend of alkaline HOR activity, verifying that the enhanced OHBE was conducive to promoting alkaline HOR kinetics.

3.3. Theoretical study

To clarify the improvement of alkaline HOR on Ru-RuS₂@C heterostructure, density functional theory (DFT) calculations were performed to elucidate the mechanism and active sites [45]. The interface based on Ru (001) and RuS₂ (200) direction was established to simulate the Ru-RuS₂ heterostructure. Three types of theoretical models for Ru-RuS₂@C heterostructure, RuS₂@C, and Ru@C were shown in Fig. S21. The charge-density distribution disclosed that electron accumulation occurred at the Ru-RuS₂ heterointer-

face (Fig. 5a), suggestive of a strong bonding effect between RuS₂ and Ru components. The electronic properties of the Ru-RuS₂@C, RuS₂@C, and Ru@C were inspected through the density of states (DOS). The calculated DOS was consecutive near the Fermi level, revealing the intrinsic metallic property on three studied electrocatalysts (Fig. 5b) [46]. Among them, Ru-RuS₂@C possessed more electronic states spanning the Fermi level, showing the enhanced conductivity, improved electron transport capability, and faster kinetics in HOR process [47]. Based on the *d*-band theory, the position of the *d*-band center reflected the binding strength of adsorption intermediate [40]. Compared to RuS₂@C (-1.37 eV) and Ru@C (-2.69 eV), Ru-RuS₂@C exhibited an appropriate *d*-band center at -1.65 eV (Fig. 5c), which can adjust the H intermediate adsorption/desorption behavior, balancing and boosting the HOR catalytic characterization [48]. According to Sabatier's principle, the free energy ΔG_{H^*} of an ideal HOR electrocatalyst should be close to zero. Although the specific reaction mechanism of basic HOR was still controversial, it was increasingly believed that the adsorbed hydroxyl group (OH^*) played a crucial role in promoting the formation of water, which was a key step in alkaline HOR. Therefore, HBE and OHBE were considered as two vital descriptors on alkaline HOR. Fig. 5(d) and Figs. S22 and S23 displayed the preferential adsorption sites of H and OH, as well as the optimized configurations on Ru-RuS₂@C, RuS₂@C, and Ru@C. Among them, the HBE values of Ru and RuS₂@C are -0.43 and 0.36 eV, respectively, indicating that their Ru surfaces had strong HBE thus leading to poor HOR performance, which was consistent with previous studies [32,49]. Meanwhile, the HBE values of Ru-RuS₂@C was -0.07 eV close to zero, implying a favorable HOR process. In addition, the hydroxyl group adsorption capacity on RuS₂@C and Ru@C was too weak, with OHBE values of 0.08 and 0.31 eV, respectively,

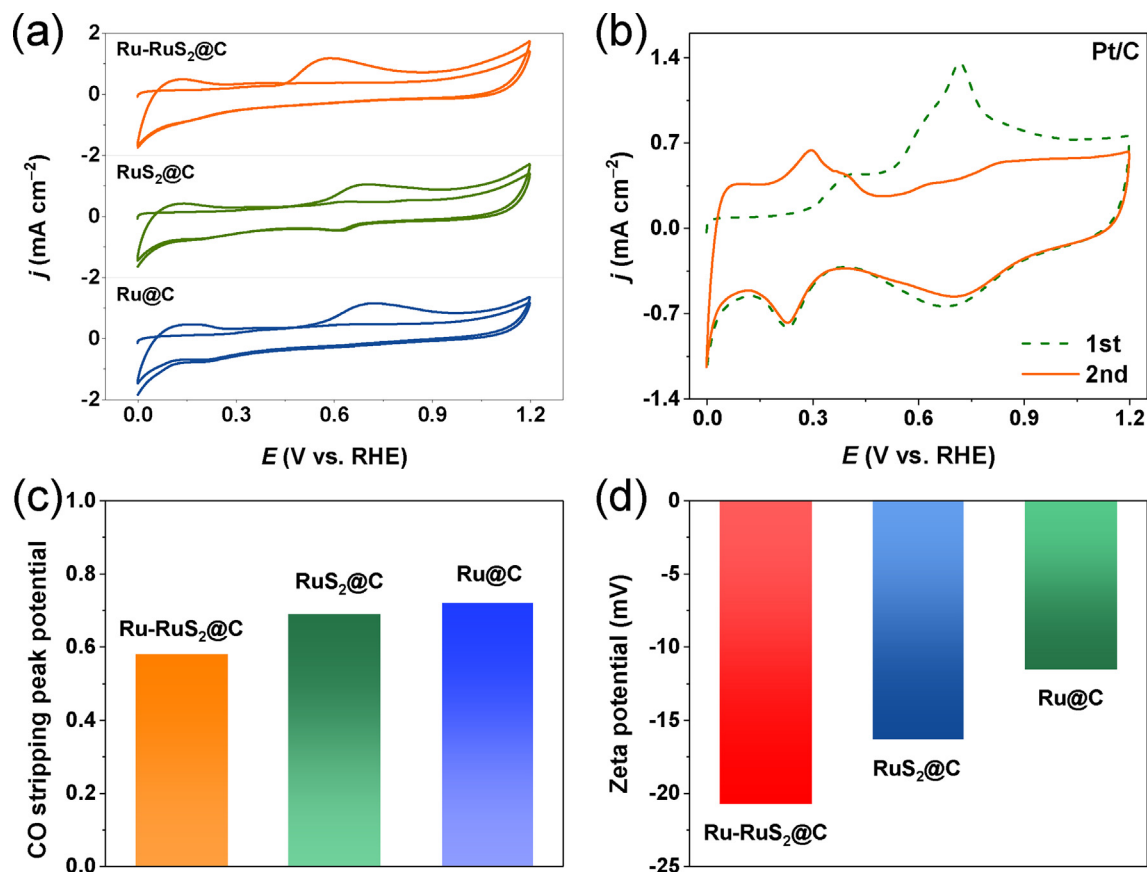


Fig. 4. CO stripping curves in CO-saturated 0.1 M KOH of different studied catalysts. (a) Ru-RuS₂@C, RuS₂@C, and Ru@C. (b) Pt/C. (c) CO stripping peak potential and (d) zeta potential of Ru-RuS₂@C, RuS₂@C, and Ru@C.

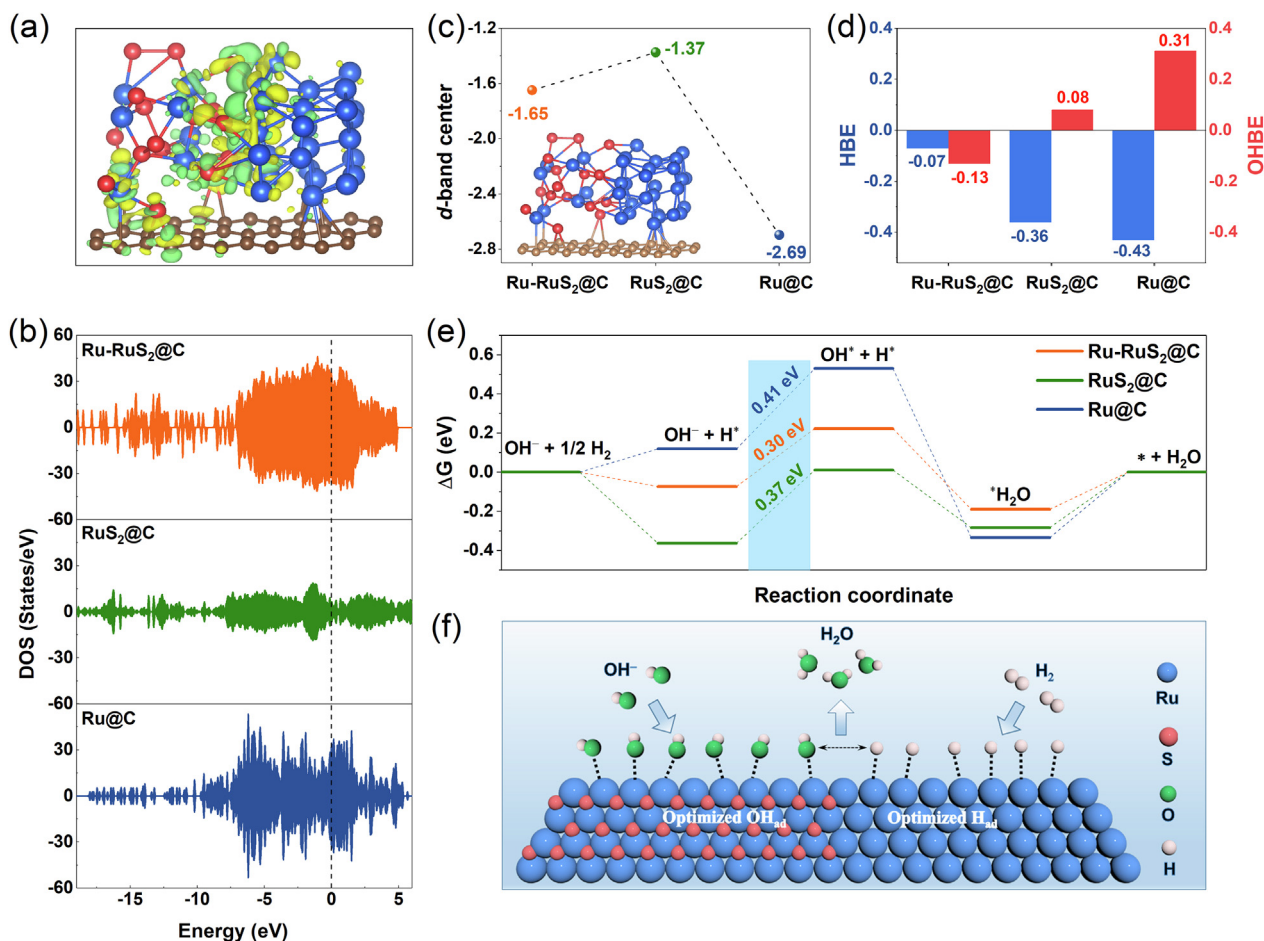


Fig. 5. (a) Charge-density distribution of the Ru-RuS₂@C model. (b) The density of state (DOS) plots. (c) The *d*-band center value of Ru in Ru-RuS₂@C, RuS₂@C, and Ru@C. (d) Calculated HBEs and OHBEs value on Ru-RuS₂@C, RuS₂@C, and Ru@C models. (e) Gibbs free energy profiles of basic HOR on the surfaces of Ru-RuS₂@C, RuS₂@C, and Ru@C. (f) Schematic illustration of the basic HOR mechanism on Ru-RuS₂@C.

which hindered the catalytic effect of HOR. As a comparison, the OHBE value of Ru-RuS₂@C was -0.13 eV, indicating that the Ru-RuS₂@C heterostructure possessed a stronger OH adsorption capacity. Such enhanced OH* adsorption behavior will facilitate the trapping of OH* species on Ru-RuS₂@C surface, thereby accelerating the Volmer step in alkaline HOR process through a bifunctional mechanism.

Previous advances demonstrated that alkaline HOR process generally abided by the Tafel-Volmer mechanism, i.e., the adsorption of H species ($\text{H}_2 \rightarrow 2\text{H}_{\text{ad}}$) followed by the formation of water ($\text{H}_{\text{ad}} + \text{OH}^- \rightarrow \text{H}_2\text{O} + \text{e}^-$) [50,51]. Therefore, we calculated the Gibbs free energy of the HOR process on three models of Ru-RuS₂@C, RuS₂@C, and Ru@C (Fig. 5e). The $\text{H}^* + \text{OH}^*$ and water desorption steps for Ru-RuS₂@C were endothermic, while the water formation was exothermic, following the same trend as RuS₂@C and Ru@C. On this basis, OH adsorption steps were considered as the rate determining step (RDS) for three studied catalysts. Ru-RuS₂@C exhibited the lowest energy barriers of 0.30 eV among those, which associated with its augmented OHBE. Consequently, the remarkable HOR performance of Ru-RuS₂@C was mainly owing to the stronger OHBE and lower RDS energy, which originated from the electron interaction between RuS₂ and Ru species. Integrating the above results, it can be concluded that the charge redistribution at the Ru-RuS₂ heterointerface synergistically optimized the adsorption of H and OH species, thereby boosting the basic HOR kinetics (Fig. 5f).

Taken together, Ru-RuS₂@C delivered robust HOR electrocatalytic properties owing to following combined effects. Firstly, the hollow mesoporous spherical structure of Ru-RuS₂@C provided an active cavity for the reactants, shortening the ion transport path and promoting HOR kinetics [25,52]. Secondly, the strong electronic interaction between RuS₂ and Ru species tuned the electronic structure, leading to accelerated electron/mass transport and fast reaction kinetics, lowering the energy barrier [53]. Thirdly, the disparate work functions on the heterostructure brought about the spontaneous formation of a unique built-in electric field, which expedited charge transfer and enhanced the conductivity of the electrocatalyst [54]. Finally, the synergistic interplay of moderate HBE and OHBE at the Ru-RuS₂@C heterogeneous interface gave great impetus to the Volmer step, which was the rate determining step in alkali HOR process [3,55].

4. Conclusions

In summary, we successfully demonstrated the effectiveness of Ru-RuS₂@C heterostructure as an efficient electrocatalyst for HOR in alkaline environment. The fabricated Ru-RuS₂@C exhibited impressive HOR performance with significantly high exchange current density and electrochemical surface area, surpassing its counterparts and even the commercial Pt/C catalyst. The distinctive features of Ru-RuS₂@C were attributed to the synergistic

interaction between Ru and RuS₂ at the heterointerface, leading to a redistribution of surface charge density. This redistribution was proven to optimize the adsorption of H and OH species, which were critical factors in enhancing the kinetics of the basic HOR process. DFT calculations further supported the experimental results, confirming that the Ru-RuS₂@C heterostructure possessed appropriate binding energies for H and OH species and exhibited a lower energy barrier for the RDS in the HOR process compared to the other studied catalysts. Moreover, Ru-RuS₂@C demonstrated admirable long-term stability and high tolerance to CO, making it a promising candidate for practical applications in fuel cells. Therefore, this work provided valuable insights into the design of advanced catalysts for efficient hydrogen fuel utilization, contributing to the advancement of a low-carbon-emission hydrogen economy.

Declaration of competing interest

The authors declare that they have no known competing financial interests or personal relationships that could have appeared to influence the work reported in this paper.

Acknowledgments

This work was financially supported by the National Natural Science Foundation of China (52363028), the Natural Science Foundation of Guangxi Province (2021GXNSFAA076001), and the Guangxi Technology Base and Talent Subject (GUIKE AD23023004, GUIKE AD20297039).

Appendix A. Supplementary material

Supplementary material to this article can be found online at <https://doi.org/10.1016/j.jechem.2024.03.007>.

References

- [1] J.A. Turner, *Science* 305 (2004) 1103197.
- [2] M. Luo, J. Yang, X. Li, M. Eguchi, Y. Yamauchi, Z.-L. Wang, *Chem. Sci.* 14 (2023) 3400–3414.
- [3] Y. Yang, Y. Huang, S. Zhou, Y. Liu, L. Shi, T. Taylor Isimjan, X. Yang, *J. Energy Chem.* 72 (2022) 395–404.
- [4] Y. Wang, Y. Yang, S. Jia, X. Wang, K. Lyu, Y. Peng, H. Zheng, X. Wei, H. Ren, L. Xiao, J. Wang, D.A. Muller, H.D. Abruna, B.J. Hwang, J. Lu, L. Zhuang, *Nat. Commun.* 10 (2019) 1506.
- [5] Y. Duan, X.L. Zhang, F.Y. Gao, Y. Kong, Y. Duan, X.T. Yang, X.X. Yu, Y.R. Wang, S. Qin, Z. Chen, R. Wu, P.P. Yang, X.S. Zheng, J.F. Zhu, M.R. Gao, T.B. Lu, Z.Y. Yu, S.H. Yu, *Angew. Chem. Int. Ed.* 62 (2023) e202217275.
- [6] S. Deng, X. Liu, X. Guo, T. Zhao, Y. Lu, J. Cheng, K. Chen, T. Shen, Y. Zhu, D. Wang, *J. Energy Chem.* 54 (2021) 202–207.
- [7] L. Gao, Y. Wang, H. Li, Q. Li, N. Ta, L. Zhuang, Q. Fu, X. Bao, *Chem. Sci.* 8 (2017) 5728–5734.
- [8] C. Long, K. Wang, Y. Shi, Z. Yang, X. Zhang, Y. Zhang, J. Han, Y. Bao, L. Chang, S. Liu, Z. Tang, *Inorg. Chem. Front.* 6 (2019) 2900–2905.
- [9] Y. Liu, L. Cheng, Y. Huang, Y. Yang, X. Rao, S. Zhou, T. Taylor Isimjan, X. Yang, *ChemSusChem* 16 (2023) e202202113.
- [10] Y. Dong, Q. Sun, C. Zhan, J. Zhang, H. Yang, T. Cheng, Y. Xu, Z. Hu, C.W. Pao, H. Geng, X. Huang, *Adv. Funct. Mater.* 33 (2022) 2210328.
- [11] X. Yang, B. Ouyang, P. Shen, Y. Sun, Y. Yang, Y. Gao, E. Kan, C. Li, K. Xu, Y. Xie, *J. Am. Chem. Soc.* 144 (2022) 11138–11147.
- [12] X. Zhang, Z. Li, X. Sun, L. Wei, H. Niu, S. Chen, Q. Chen, C. Wang, F. Zheng, *ACS Mater. Lett.* 4 (2022) 2097–2105.
- [13] S. Ni, H. Qu, Z. Xu, X. Zhu, H. Xing, L. Wang, J. Yu, H. Liu, C. Chen, L. Yang, *Appl. Catal. B: Environ.* 299 (2021) 120638.
- [14] L. Su, D. Gong, Y. Jin, D. Wu, W. Luo, *J. Energy Chem.* 66 (2022) 107–122.
- [15] X. Wang, L. Zhuang, Y. Jia, H. Liu, X. Yan, L. Zhang, D. Yang, Z. Zhu, X. Yao, *Angew. Chem. Int. Ed.* 57 (2018) 16421–16425.
- [16] X. Zhao, H. Zhang, Y. Yan, J. Cao, X. Li, S. Zhou, Z. Peng, J. Zeng, *Angew. Chem. Int. Ed.* 56 (2017) 328–332.
- [17] H. Wang, Y. Liang, S. Liu, X. Mu, H. Yu, K. Deng, Z. Wang, Y. Xu, L. Wang, *Inorg. Chem. Front.* 10 (2023) 5686–5693.
- [18] L. Su, Y. Jin, D. Gong, X. Ge, W. Zhang, X. Fan, W. Luo, *Angew. Chem. Int. Ed.* 62 (2022) e202215585.
- [19] Z. Huang, Z. Liu, M. Liao, L. Wang, Z. Luo, T.T. Isimjan, X. Yang, *Chem. Eng. J.* 462 (2023) 142281.
- [20] X. Gao, B. Li, X. Sun, B. Wu, Y. Hu, Z. Ning, J. Li, N. Wang, *Chin. Chem. Lett.* 32 (2021) 3591–3595.
- [21] P. Li, W. Li, Y. Huang, J. Li, Q. Huang, S. Zhao, S. Tian, *Nanoscale* 14 (2022) 6258–6267.
- [22] J. Zhu, S. Mu, *Inorg. Chem. Front.* 10 (2023) 2220–2225.
- [23] Y. Li, C. Yang, J. Yue, H. Cong, W. Luo, *Adv. Funct. Mater.* 33 (2023) 2211586.
- [24] S. Gong, W. Wang, C. Zhang, M. Zhu, R. Lu, J. Ye, H. Yang, C. Wu, J. Liu, D. Rao, S. Shao, X. Lv, *Adv. Funct. Mater.* 32 (2022) 2110649.
- [25] M. Guo, Z. Huang, Y. Qu, L. Wang, H. Li, T.T. Isimjan, X. Yang, *Appl. Catal. B Environ.* 320 (2023) 121991.
- [26] M. Guo, M. Xu, Y. Qu, C. Hu, P. Yan, T.T. Isimjan, X. Yang, *Appl. Catal. B: Environ.* 297 (2021) 120415.
- [27] X. Zhao, X. Yu, S. Xin, S. Chen, C. Bao, W. Xu, J. Xue, B. Hui, J. Zhang, X. She, D. Yang, *Appl. Catal. B Environ.* 301 (2022) 120785.
- [28] X.F. Lu, L. Yu, J. Zhang, X.W. Lou, *Adv. Mater.* (2019) 1900699.
- [29] K. Shah, R. Dai, M. Mateen, Z. Hassan, Z. Zhuang, C. Liu, M. Israr, W.C. Cheong, B. Hu, R. Tu, C. Zhang, X. Chen, Q. Peng, C. Chen, Y. Li, *Angew. Chem. Int. Ed.* 61 (2022) 202114951.
- [30] M. Sarno, E. Ponticorvo, *Int. J. Hydrogen Energy* 44 (2019) 4398–4405.
- [31] Y. Zhao, F. Yang, W. Zhang, Q. Li, X. Wang, L. Su, X. Hu, Y. Wang, Z. Wang, L. Zhuang, S. Chen, W. Luo, *CCS Chem.* 4 (2021) 1732–1744.
- [32] Z. Cheng, Y. Yang, P. Wang, P. Wang, J. Yang, D. Wang, Q. Chen, *Small n/a* (2024) 2307780.
- [33] C. Yang, Y. Li, J. Yue, H. Cong, W. Luo, *Chem. Sci.* 14 (2023) 6289–6294.
- [34] Y. Yang, X. Shao, S. Zhou, P. Yan, T.T. Isimjan, X. Yang, *ChemSusChem* 14 (2021) 2992–3000.
- [35] G. Meng, H. Cao, T. Wei, Q. Liu, J. Fu, S. Zhang, J. Luo, X. Liu, *Chem. Commun.* 58 (2022) (1842) 11839–11831.
- [36] J. Wu, Y. Zhou, H. Nie, K. Wei, H. Huang, F. Liao, Y. Liu, M. Shao, Z. Kang, *J. Energy Chem.* 66 (2022) 61–67.
- [37] D.Q. Liu, Z. Luo, B. Zhang, G. Zhao, W. Guo, J. Chen, M. Gao, Y. Liu, H. Pan, W. Sun, *Adv. Funct. Mater.* 13 (2022) 2202913.
- [38] M. Fang, Y. Ji, S. Geng, J. Su, Y. Li, Q. Shao, J. Lu, *ACS Appl. Nano Mater.* 5 (2022) 17496–17502.
- [39] Y. Pi, Z. Qiu, Y. Sun, H. Ishii, Y.F. Liao, X. Zhang, H.Y. Chen, H. Pang, *Adv. Sci.* 10 (2023) 2206096.
- [40] L. Su, Y. Zhao, Y. Jin, X. Fan, Z. Liu, W. Luo, *J. Mater. Chem. A* 10 (2022) (1861) 21856–121852.
- [41] Y. Men, X. Su, P. Li, Y. Tan, C. Ge, S. Jia, L. Li, J. Wang, G. Cheng, L. Zhuang, S. Chen, W. Luo, *J. Am. Chem. Soc.* 144 (2022) 12661–12672.
- [42] B. Qin, H. Yu, X. Gao, D. Yao, X. Sun, W. Song, B. Yi, Z. Shao, *J. Mater. Chem. A* 6 (2018) 20374–20382.
- [43] Y. Wang, G. Wang, G. Li, B. Huang, J. Pan, Q. Liu, J. Han, L. Xiao, J. Lu, L. Zhuang, *Energy Environ. Sci.* 8 (2015) 177–181.
- [44] S. Lyu, C. Guo, J. Wang, Z. Li, B. Yang, L. Lei, L. Wang, J. Xiao, T. Zhang, Y. Hou, *Nat. Commun.* 13 (2022) 6171.
- [45] C. Huang, M. Feng, Y. Peng, B. Zhang, J. Huang, X. Yue, S. Huang, *Adv. Funct. Mater.* 33 (2023) 2300593.
- [46] X. Xu, C. Zhang, J. Li, H. Liu, G. Su, Z. Shi, M. Huang, *Chem. Eng. J.* 452 (2023) 139362.
- [47] D. Chen, R. Yu, R. Lu, Z. Pu, P. Wang, J. Zhu, P. Ji, D. Wu, J. Wu, Y. Zhao, Z. Kou, J. Yu, S. Mu, *InfoMat* 4 (2022) e12287.
- [48] C. He, Q. Liu, H. Wang, C. Xia, F.M. Li, W. Guo, B.Y. Xia, *Small* 19 (2023) 2207474.
- [49] J. Liu, J. Wang, Y. Fo, B. Zhang, C. Molochas, J. Gao, W. Li, X. Cui, X. Zhou, L. Jiang, P. Tsiakaras, *Chem. Eng. J.* 454 (2023) 139959.
- [50] M. Ma, G. Li, W. Yan, Z. Wu, Z. Zheng, X. Zhang, Q. Wang, G. Du, D. Liu, Z. Xie, Q. Kuang, L. Zheng, *Adv. Energy Mater.* 12 (2022) 2103336.
- [51] S. Lu, Z. Zhuang, *J. Am. Chem. Soc.* 139 (2017) 5156–5163.
- [52] Y. Guo, J. Tang, H. Qian, Z. Wang, Y. Yamauchi, *Chem. Mater.* 29 (2017) 5566–5573.
- [53] R. Boppella, J. Tan, W. Yang, J. Moon, *Adv. Funct. Mater.* 29 (2018) 1807976.
- [54] J. Li, J. Hu, M. Zhang, W. Gou, S. Zhang, Z. Chen, Y. Qu, Y. Ma, *Nat. Commun.* 12 (2021) 3502.
- [55] Y. Qiu, L. Xin, Y. Li, I.T. McCrum, F. Guo, T. Ma, Y. Ren, Q. Liu, L. Zhou, S. Gu, M.J. Janik, W. Li, *J. Am. Chem. Soc.* 140 (2018) 16580–16588.